Electrodynamics of ferroelectric films with negative capacitance

I. Luk'yanchuk,[1,2] A. Sené,[1] and V. M. Vinokur[3]
[1]*Laboratory of Condensed Matter Physics, University of Picardie, Amiens, 80039, France*
[2]*Landau Institute for Theoretical Physics, Akademika Semenova av., 1-A, Chernogolovka, 142432, Russia*
[3]*Materials Science Division, Argonne National Laboratory, 9700 S. Cass Avenue, Argonne, Illinois 60439, USA*

(Received 10 February 2018; revised manuscript received 23 April 2018; published 27 July 2018)

We construct a theory of the electrodynamic response of ferroelectric thin films containing periodic domain textures (PDTs) with 180° polarization-oriented domains. We demonstrate that a depolarization field induced by PDTs gives rise to the negative capacitance of the ferroelectric film. We derive frequency-dependent dielectric permittivity related to the PDT dynamics across the entire frequency range. We find the resonance mode of domain oscillations in the terahertz (THz) spectral band and the singular points in the phase of the reflected THz beam that are intimately related to the negative capacitance. Our findings provide a material platform for the THz negative-capacitance-based optics of ferroelectric films and for epsilon-near-zero plasmonic THz metamaterials.

DOI: 10.1103/PhysRevB.98.024107

I. INTRODUCTION

Functional properties of ferroelectric films and superlattices are drastically different from those of the bulk materials. Extensive experimental [1–7] and theoretical [8–14] studies revealed new physics that emerges from the periodic domain textures (PDTs) stabilized by the strains and the depolarization fields. One of the most striking features of the PDTs is the manifestation of negative capacitance [15], a phenomenon that has been the subject of intense recent attention [16–22]. The interest is motivated by both its fundamental importance and its high potential for technological applications, in particular, as a platform for novel low-dissipation field-effect transistors.

Another facet of emergent functionalities of ferroelectric films arises due to the strain tunability of their multiscale spontaneous polarization dynamics that provides a wide range of operational frequencies from a few kilohertz to tens of terahertz ($1\,\mathrm{THz} = 10^{12}\,\mathrm{Hz}$). The spectral band $10^4\,\mathrm{Hz}$ to 0.3 THz is covered by the relaxation dynamics of the domain walls (DWs) and polar clusters. The far-infrared spectral region of 3–30 THz is governed by the soft-mode vibrations of the polar ions. Recent studies suggested that oscillations of DWs in PDTs occur in the frequency window of 0.3–3 THz [23–25], i.e., within the least studied frequency range, referred to as a THz gap.

Our work steps into the breach and demonstrates that the resonant behavior of oscillations of PDTs is a collective effect similar to plasmonic excitations in metals. We find that this effect is governed by the stiffness of PDTs promoted by the depolarization field and is a consequence of the negative capacitance. Namely, the negative low-frequency effective permittivity associated with the negative capacitance crosses the zero value within the THz spectrum band, leading to a resonance behavior in complete analogy with the plasmon resonance. We investigate the THz optics of the PDT structure and demonstrate the existence of the topologically protected phase-singular points of the absolute darkness in the Fresnel reflection coefficient. These points are a fingerprint of the negative-capacitance phenomenon.

Formation of the PDT lowers the energy of the depolarization field induced by surface depolarization charges that appear at polarization termination points. Had the polarization maintained the same direction throughout the slab [see Fig. 1(a)], the electrostatic energy stored by the depolarization field would be proportional to the volume of the whole system and hence huge. Splitting the system into the PDT implies that the surface depolarization charges assume the form of stripes with alternating signs. As a result, the depolarization field becomes restricted to the near-surface shell [see Fig. 1(b)], hence drastically diminishing the related electrostatic energy. Although predicted already in earlier works by Landau and Lifshitz [26,27] and Kittel [28] in the context of ferromagnetic systems, the PDT in ferroelectric films has long been viewed as unlikely until the recent direct experimental evidence of equilibrium 180° stripe domains in strained ferroelectric thin films of $PbTiO_3$ (PTO) deposited on a $SrTiO_3$ (STO) substrate [1,6] [as sketched in Fig. 1(b)] and in PTO/STO superlattices [3,5] [Fig. 1(c)]. The observed PDT behaviors appeared to follow the theoretical predictions well [8–14]. In particular, it was found that the monodomain z-oriented state in the unscreened films is always unstable with respect to the PDT formation.

Imagine, however, that surfaces of the slab get short-circuited, for example, by the metallic electrodes. Then charges would acquire the capability of arbitrary sliding along the surfaces and flowing between the electrodes, thus compensating the depolarization field inside the ferroelectric. As a result, the depolarization energy is nullified, the domain walls creep away, and the monodomain state stabilizes. This tendency of a ferroelectric with the PDT to self-generate the charge at its surfaces can be expressed by attributing to the ferroelectric slab a *negative* capacitance. One should bear in mind, however, that in reality, a slab that is not linked to the electrodes maintains the PDT since charges cannot propagate across the dielectric and the charge redistribution described above would not occur.

The origin of the negative capacitance is as follows [see Fig. 1(d)]. In the absence of the applied electric field, the up- and down-directed domains are of equal size; hence, both the

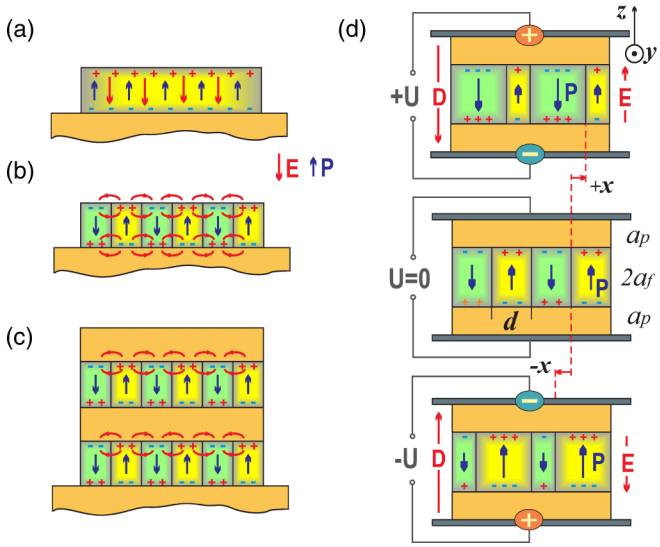

FIG. 1. Formation and dynamics of the periodic domain texture (PDT). (a) A single-domain state, the ferroelectric polarization and the depolarization field are shown by the blue and red arrows, respectively. The depolarization field traverses across the film. (b) The PDT with the alternating 180° polarization domains. The depolarization field is confined to the surface of the film. (c) A sketch of the ferroelectric-paraelectric superlattice with PDT. (d) The response of the PDT structure to variations of the voltage U applied to the ferroelectric-paraelectric system. The applied voltage induces the electric displacement $\mathbf{D}$ satisfying the continuity condition across the entire system. The average electric field $\mathbf{E}$ within the ferroelectric film is directed opposite the induced average polarization $\mathbf{P}$ and displacement $\mathbf{D}$. This manifests the effect of the negative capacitance. Stray fields are not shown in order to avoid an overcrowded picture.

average polarization and the average depolarization field are zero. The applied electric field displaces DWs, unbalancing the sizes of the domains, which results in the onset of the average polarization, oriented along the applied field. This, in turn, generates the depolarization field penetrating the bulk of the ferroelectric slab from the surface. The direction of the depolarization field is opposite the polarization and hence to the applied field and exceeds the latter by the absolute value. As a result, the total field inside the slab is counterdirected to the induced polarization, which is a hallmark of the negative permittivity, hence the negative capacitance of the ferroelectric layer.

We calculate the permittivity of the PDT and explicitly demonstrate that it assumes a negative value in the static limit. Then, writing down the coupled PDT equations of motion and Maxwell equations, we derive the frequency dependence of the permittivity of the PDT in the entire frequency range and find the corresponding resonance mode. We show that this mode arises in the frequency band where the negative permittivity changes sign. Finally, based on the calculated frequency dependence of the permittivity, we derive the THz optical properties of the ferroelectric layer.

II. RESULTS

A. Negative capacitance

We start the description of the domain electrodynamics with the static limit and show that the PDT in response to the applied field develops the fascinating negative dielectric permittivity ε_f and, accordingly, the effective negative capacitance, $C = \varepsilon_0\varepsilon_f S/(2a_f)$, of the ferroelectric layer of surface area S and thickness $2a_f$.

The applied field is characterized by the electric displacement vector $\mathbf{D}$ that is conserved all across the system [see Fig. 1(d)] and generates the net polarization of the ferroelectric layer, $\mathbf{P} \parallel \mathbf{z}$ (the electrostatic fields in the ferroelectric slab with domains are macroscopically averaged). In our ferroelectric film the electric displacement is related to the electric field through

$$\mathbf{D} = \varepsilon_0\varepsilon_\parallel \mathbf{E} + \mathbf{P}_{\rm dw}. \tag{1}$$

Note that in the absence of the applied field, both terms on the right-hand side of Eq. (1) are zero. The contribution $\mathbf{P}_{\rm dw}$ stems from the motion of the domain walls. In the absence of the motion, Eq. (1) reduces to the standard electrostatic relation between the electric field and electric displacement. The dielectric constant $\varepsilon_\parallel$ is the intrinsic permittivity of the ferroelectric material along the polarization direction. The $\mathbf{P}_{\rm dw}$ term reflects the change in the overall polarization due to the displacement of the DWs, thus altering the relative contribution from the "up"- and "down"-oriented domains. This implies the imbalance of the related depolarization charges of the opposite sign leading to the nonzero average charge density $\sigma = P_{\rm dw}$. Thus, the depolarization field $\mathbf{E}_{\rm dep} = -(\varepsilon_0\varepsilon_\parallel)^{-1}\mathbf{P}_{\rm dw}$ penetrates the bulk of the slab and is directed opposite the applied field $\mathbf{D}$. This field, together with the driving field $\mathbf{E}_{\rm D} = (\varepsilon_0\varepsilon_\parallel)^{-1}\mathbf{D}$, which would settle down if the DWs were immobile, contributes to the total field, $\mathbf{E} = \mathbf{E}_{\rm D} + \mathbf{E}_{\rm dep}$. Hence, the sign of the system's dielectric permittivity, which is defined as

$$\varepsilon_{\rm f} = \frac{D}{\varepsilon_0 E}, \tag{2}$$

depends on the relative magnitude of the oppositely oriented $\mathbf{E}_{\rm D}$ and $\mathbf{E}_{\rm dep}$.

Making use of the relation (1), one obtains

$$\varepsilon_{\rm f} = \frac{\varepsilon_\parallel D}{D - P_{\rm dw}}. \tag{3}$$

To derive ε_f, we have to know how the polarization related to the DW displacement depends on the applied field D. The calculations presented in the Appendix result in

$$\varepsilon_{\rm f} = \varepsilon_\parallel - \frac{\pi\varsigma}{4\ln 2}\left(\frac{\varepsilon_\perp}{\varepsilon_\parallel}\right)^{1/2}\frac{2a_{\rm f}}{d}\varepsilon_\parallel, \tag{4}$$

where the first term stems from the positive intrinsic contribution of $\mathbf{E}_{\rm D}$, whereas the second term, the negative one, is generated by the depolarizing field $\mathbf{E}_{\rm dep}$, reflecting the effect of the moving DW. The depolarizing term outweighs the intrinsic term; hence, the negative dielectric permittivity settles, provided the film thickness $2a_{\rm f}$ exceeds the domain width d. The equilibrium value of d can be either taken from the experiment [1,5] or estimated by the Landau-Kittel square-root law [26–28] specifically adapted for ferroelectrics in [8,12,29],

$$d \simeq \sqrt{3.53(\varepsilon_\perp/\varepsilon_\parallel)^{1/2}\varsigma\delta 2a_{\rm f}}. \tag{5}$$

The resulting typical domain configuration for PTO films is shown in Fig. 1(b). The DW thickness δ is about 1 nm [30]. In the above formulas $\varsigma = 1 + \varepsilon_p/(\varepsilon_\parallel \varepsilon_\perp)^{1/2}$, and the values of intrinsic permittivities along and across the polarization direction, $\varepsilon_\parallel$ and $\varepsilon_\perp$, and of the paraelectric layer, ε_p, are specified below; in the experimental range $1 \leqslant \varsigma \leqslant 4$. If the sandwiching paraelectric layers possess different permittivities, ε_p^+ and ε_p^-, the effective parameter $\varsigma_{\rm eff}$ is defined by the relation $\varsigma_{\rm eff}^{-1} = \frac{1}{2}[\varsigma^{-1}(\varepsilon_p^+) + \varsigma^{-1}(\varepsilon_p^-)]$. In particular, if the ferroelectric film is deposited on the metallic substrate so that $\varepsilon_p^- = 1$ and $\varepsilon_p^+ = \infty$, one has $\varsigma_{\rm eff} \simeq 2$. The polarization profile in this case can be obtained with the image method.

B. DW oscillations

To quantify the electromagnetic behavior of PDTs, we derive the dynamic response function $\gamma(\omega)$, defined by the relation $\mathbf{P}_{{\rm dw}\,\omega} = \gamma(\omega)\mathbf{D}_\omega$, for the periodic structure of the domain stripes aligned along the **y** axis which forms in the ferroelectric layer. The polarization axis, **z**, is perpendicular to the film plane, while the in-plane DW motion occurs along the **x** axis and the index ω indicates the Fourier transforms of the respective quantities. We neglect the longitudinal DW fluctuations, which can broaden the resonance peak [31].

In the harmonic oscillator approximation [32] the driven dynamics of DWs is given by

$$\mu\ddot{x}(t) + \eta\dot{x}(t) + kx(t) = 2P_s E_D(t), \tag{6}$$

where x is the coordinate of alternating DW displacements [Fig. 1(d)], the coefficients k, μ, and η are calculated per unit of DW area, and $2P_s E_D(t)$ is the pressure due to the electric displacement-induced driving field forcing the DW to move to flip the surrounding spontaneous polarization from $-P_s$ to $+P_s$.

We calculate k as a coefficient at the restoring force that pushes the domain walls back in order to reduce the depolarization field, $E_{\rm dep} = -\Delta P_s/\varepsilon_0 = -2(x/\varepsilon_0 d)P_s$, arising upon the displacement of the DW from equilibrium. This field is induced by the extra depolarization surface charges, $\sigma = \pm\Delta P_s$, appearing due to the spontaneous polarization excess, $\Delta P_s = 2(x/d)P_s$, and is directed antiparallel to ΔP_s. We evaluate the depolarization energy of the system as the electrostatic energy of the dielectric slab with permittivity $\varepsilon_\parallel$ and with surface charges $\sigma = 2(x/d)P_s$ as $W = (2a_f\sigma^2/2\varepsilon_0\varepsilon_\parallel)S$, where S is the surface area. The corresponding energy per unit area of the displaced DW is $w = (d/2Sa_f)W$. Relating it to the harmonic oscillator stiffness energy $kx^2/2$, we find

$$k = \frac{4P_s^2}{\varepsilon_0\varepsilon_\parallel d}g, \quad g \simeq 1 - \frac{4\ln 2}{\pi\varsigma}\left(\frac{\varepsilon_\parallel}{\varepsilon_\perp}\right)^{1/2}\frac{d}{2a_f}. \tag{7}$$

The factor g, calculated in the Appendix and confined to the interval $0 < g \lesssim 1$, takes into account the nonuniform part of the depolarization field near the surface caused by the stepwise distribution of the depolarization surface charges. In the realistic cases that we consider here, namely, PTO films with $2a_f \simeq$ 10–30 nm, it varies from 0.4 to 0.9.

Equation (6) presumes that the DW is rigid and atomically narrow. However, in thin films tens of nanometers thick the DW broadens significantly, especially when approaching the film surface, due to depolarization effects in the broad range of temperatures (yet the effective thickness of the DWs remains smaller than the distance between them as long as the model holds) [12,14,33,34]. Upon the DW displacement, the polarization first reverses at the surface and then propagates into the interior of the film [23]. As a result of the DW broadening, the underlying pinning potential for the DW due to the periodic atomic structure gets essentially reduced and becomes relevant only at low temperatures.

In general, the PDT can be viewed as a meandering two-dimensional crystal with the spatially nearly random in-plane orientation of stripes [4]. The elasticity of such a structure is described by the Landau-Peierls elastic free energy, which is similar to that of the layered liquid crystal, smectic-A [35]. This implies that the compression deformations (corresponding to THz oscillations in our case) are much more rigid than the bending deformations. The latter is a generic property of layered systems following from their symmetry. As a result, the longitudinal dispersion of the PDT stiffness $k(q)$, with q being a wave vector along the DW, is small in the long-wave limit. Therefore, k is not too sensitive to the possible roughness of the DW on scales much less than the domain size, and the THz PDT oscillations can be described by the one-dimensional model given by Eq. (6). Moreover, a purely electrostatic origin of the stiffness k makes oscillations weakly sensitive to the orientation of the PDT with respect to crystallographic axes.

The effective DW mass μ and the viscosity η in Eq. (6) are related to the motion of the material-constituent polar ions during the displacement of the DWs [36] and to the piezoelectric effect of the time-varying depolarization field [32]. The magnitude of μ was calculated in *ab initio* simulations of DW dynamics in the sub-THz range [23]. We propose an interpolation formula $\mu\,[{\rm kg/m^2}] \simeq 1.3\sqrt{2a_f\,[{\rm nm}]} \times 10^{-9}$, which matches well the numerical result. Viscosity η is expressed through the damping factor of the DW motion, $\Gamma = \eta/\mu$. Since a consistent theory for Γ is not available, we chose the value of Γ that comes from the measurements of the soft-mode relaxation of polar ions, which has the characteristic damping time of the order of a few picoseconds. This time is much shorter than the typical switching time of the PDT [4] of hundreds of nanoseconds and serves therefore as a characteristic time restricting the damping of oscillatory dynamics from below.

C. THZ resonance

In what follows we calculate the complex dynamic permittivity of PDT $\varepsilon_f(\omega)$. The resulting plots of the real, ${\rm Re}\varepsilon_f(\omega)$, and imaginary, ${\rm Im}\varepsilon_f(\omega)$, parts of the dispersion $\varepsilon_f(\omega)$ for a 30-nm-thick film of PTO are shown in Fig. 2(a).

The reaction of the ferroelectric layer to the time-dependent applied field $\mathbf{D}(t) = \int d\omega\,\mathbf{D}_\omega e^{-i\omega t}$ is characterized by the linear response function $\gamma(\omega)$. Solving Eq. (6) by Fourier transformation, we find

$$\gamma(\omega) = \frac{g^{-1}\omega_0^2}{\omega_0^2 - \omega^2 - i\Gamma\omega}, \quad \omega_0 = \left(\frac{4P_s^2 g}{\mu d\varepsilon_0\varepsilon_\parallel}\right)^{1/2}, \tag{8}$$

where the characteristic oscillation frequency is the usual $\omega_0 = (k/\mu)^{1/2}$, with k and μ related to the system parameters, as discussed above. When deriving Eq. (8), we took into account that $\mathbf{P}_{{\rm dw}\,\omega} = 2P_s\,(x_\omega/d)\mathbf{z}$ and $\mathbf{D}_\omega = \varepsilon_0\varepsilon_\parallel\mathbf{E}_{{\rm D}\,\omega}$.

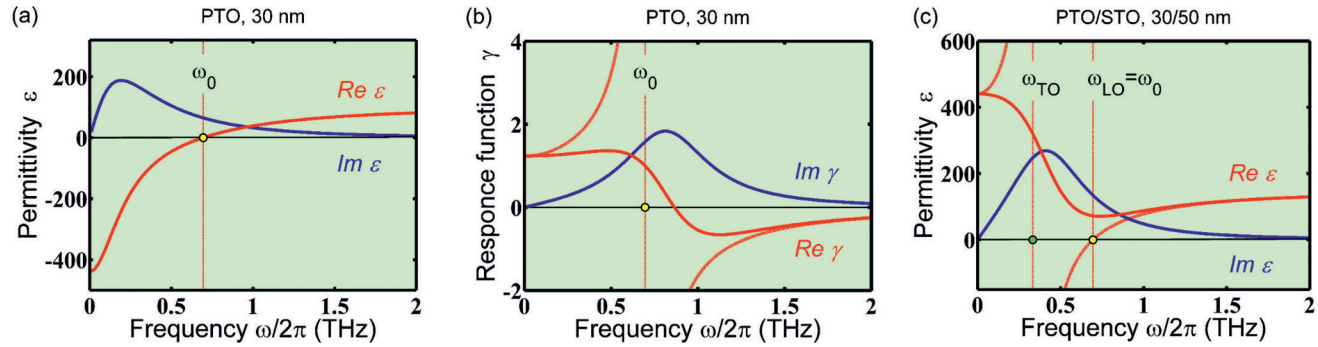

FIG. 2. Dynamical properties of the PDT. Real and imaginary parts of the frequency-dependent response are shown in red and blue, respectively. Dashed lines depict the behavior of the system in the absence of dissipation. (a) Dielectric permittivity of the 30-nm-thick film of the PTO. (b) Response function, defined as $\mathbf{P}_{\mathrm{dw}\,\omega} = \gamma(\omega)\mathbf{D}_{\omega}$, for the same film. (c) Dielectric permittivity for either the 30-/50-nm sandwich of the PTO/STO layers or the equivalent superlattice.

Shown in Fig. 2(b) are the real and imaginary parts of $\gamma(\omega)$ for our sample exhibiting a characteristic Lorentzian-type form. The latter is a legacy of a singularity at ω_0, which would have been exhibited by a system without the dissipation, illustrated by the dashed lines. The emergence of the resonance response to the applied field is clearly demonstrated by the frequency dependence of the absolute value of the response function $|\gamma(\omega)|$ for different film thicknesses [see Fig. 3(a)], reaching its maximum at the resonance frequency $\omega_{\mathrm{r}}^2 = \omega_0^2 - \Gamma^2/2$. The dependence of ω_{r} upon the film thickness $2a_{\mathrm{f}}$ is shown in Fig. 3(b). Shown by the blue line in the same panel is the Landau-Kittel dependence of the domain width d on the film thickness given by Eq. (5).

Equation (8) enables optimization of the material parameters and the film thickness to make sure that ω_{r} falls within the desired THz frequency range. In particular, for the strained films of the PTO with high spontaneous polarization, $P_s \simeq 0.65\,\mathrm{C\,m^{-2}}$ (see [37]), relatively low permittivities $\varepsilon_{\parallel} \simeq 100$ and $\varepsilon_{\perp} \simeq 30$, soft-mode damping factor $\Gamma \simeq 20\,\mathrm{cm^{-1}}$ (0.6 THz) [38], and μ defined as above, the resonance frequency ω_r decreases and spans the range from 1.5 to 0.75 THz

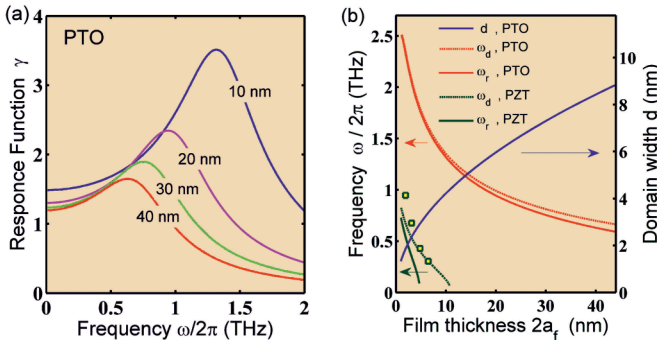

FIG. 3. Resonance in the PDT. (a) Resonance behavior of the amplitude of the response function $|\gamma(\omega)|$ for different film thicknesses of the PTO. (b) Dependence of the domain resonance frequency ω_{r}, of the damping frequency ω_{d}, and of the domain width d upon the film thickness. The solid red line stands for ω_{r} of the PTO; the dashed red line shows ω_{d} of the PTO. The solid and dashed green lines show ω_{r} and ω_{d}, respectively, for PZT. Green squares display the results of the *ab initio* simulations for PZT [23]. The blue solid line displays the behavior of the domain width d.

when $2a_{\mathrm{f}}$ increases from 10 to 40 nm. We find the damping frequency, $\omega_{\mathrm{d}}^2 = \omega_0^2 - \Gamma^2/4$, of the attenuated oscillations of domains in PTO, $x(t) = x_0 e^{-(\Gamma/2)t} \sin\omega_{\mathrm{d}} t$, which is slightly larger than ω_{r} [see Fig. 3(b)]. Remarkably, our formulas perfectly describe the results of *ab initio* simulations of DW oscillations in lead zirconic titanate (PZT) freestanding ultrathin films [23]. The calculated damping frequency ω_{d} is shown by the dashed line in Fig. 3(b); the symbols display the results of the simulations. Here we used the following parameters for PZT: $P_{\mathrm{s}} \simeq 0.40\,\mathrm{C\,m^{-2}}$ [37], $\varepsilon_{\parallel}, \varepsilon_{\perp} \simeq 350$, $\Gamma \simeq 27\ \mathrm{cm^{-1}}$ (0.8 THz) [39], and the same value for DW mass μ. At the same time, the resonance frequency of PZT ω_{r} drops rapidly with the thickness and vanishes above 4 nm. The data in this paragraph are given for ceramic samples. The values for strained films can be slightly different.

Making use of the relation $\gamma(\omega) = 1 - \varepsilon_{\parallel}/\varepsilon_{\mathrm{f}}(\omega)$ that follows directly from Eq. (1), we obtain the dynamic permittivity of a ferroelectric layer:

$$\varepsilon_{\mathrm{f}}(\omega) = \frac{\varepsilon_{\parallel}}{1-\gamma(\omega)} = \varepsilon_{\parallel}\frac{\omega_0^2 - \omega^2 - i\Gamma\omega}{(1-g^{-1})\,\omega_0^2 - \omega^2 - i\Gamma\omega}, \qquad (9)$$

with $1 - g^{-1} < 0$. At small ω this yields the negative static permittivity described by Eq. (4). We plot the real, $\mathrm{Re}\varepsilon_{\mathrm{f}}(\omega)$, and imaginary, $\mathrm{Im}\varepsilon_{\mathrm{f}}(\omega)$, parts of complex dispersion $\varepsilon_{\mathrm{f}}(\omega)$, calculated for a 30-nm-thick film of PTO in a paraelectric environment [see Fig. 2(a)]. At low frequencies $\mathrm{Re}\varepsilon_{\mathrm{f}}(\omega)$ remains negative. At high frequencies the oscillations of DWs freeze out, and therefore, $\varepsilon_{\mathrm{f}}(\omega)$ should become positive and equal to intrinsic permittivity, $\mathrm{Re}\varepsilon_{\mathrm{f}}(\infty) = \varepsilon_{\parallel} > 0$. At frequency $\omega = \omega_0$, the real part of the permittivity becomes zero, $\mathrm{Re}\varepsilon_{\mathrm{f}}(\omega_0) = 0$. This behavior of PDT permittivity resembles that of a metal with the negative real part of the permittivity below the *plasma frequency* at which it becomes equal to zero. Accordingly, this will lead to the plasma resonance at $\omega = \omega_0$ in a PDT as a response to the driving field $\mathbf{D}$.

The discovered resonance mode gives rise to the Drude-Lorentz frequency response of a biased capacitor consisting of the ferroelectric layer (of thickness $2a_{\mathrm{f}}$) sandwiched between paraelectric buffer layers (each with thickness a_{p} and permittivity ε_{p}). The same response appears in the $2a_{\mathrm{f}}/2a_{\mathrm{p}}$ ferroelectric-paraelectric superlattice. The effective permittivity, calculated for the system of in-series capacitors, $\varepsilon_{\mathrm{tot}}^{-1}(\omega) = \alpha_{\mathrm{p}}\varepsilon_{\mathrm{p}}^{-1} +$

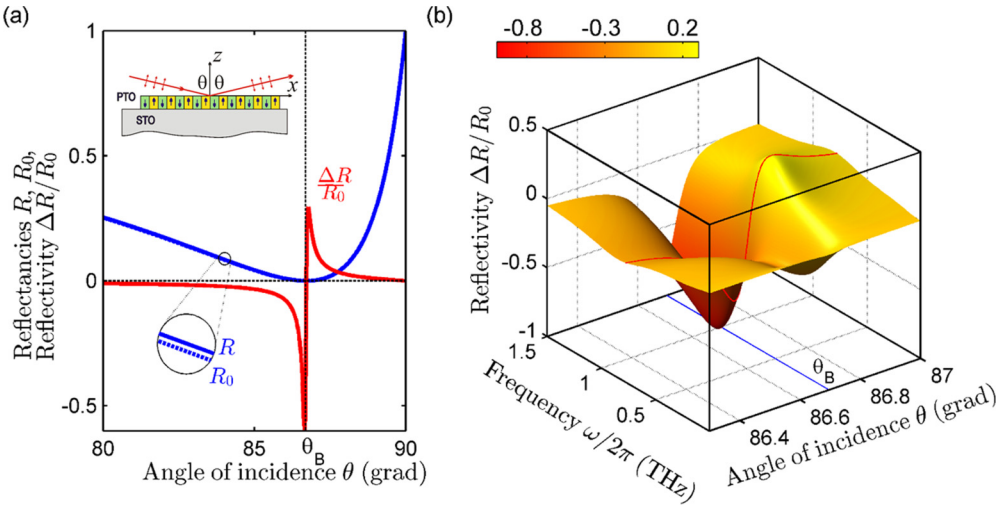

FIG. 4. Reflection characteristics of the PDT. The p-polarized THz beam reflects from the $2a_f \simeq 30$ nm thick PTO film deposited on the STO dielectric substrate. (a) The dependence of the reflectance of the film on the substrate R and the dependence of the net reflectance of the substrate R_0 on the incidence angle θ calculated at the PDT oscillation frequency $\omega_0/2\pi \simeq 0.75$ THz are shown by the blue solid and dashed lines, respectively. The difference between the two is tiny, $|\Delta R| = |R_0 - R| \lesssim 10^{-3}$, and, at the figure scale, is seen only under magnification. In contrast, the reflectivity $\Delta R/R_0$ experiences a drastic variation of about unity and clearly displays a Lorentz-like spike at the Brewster angle $\theta_B \simeq 86.7^\circ$, where R_0 almost vanishes. This spike is a fingerprint of the PDT resonance and can be used for its experimental identification. The inset shows the geometry of the experiment. (b) The 3D color plot of the reflectivity $\Delta R/R_0$ as a function of the frequency and the incident angle in the immediate vicinity of the Brewster angle θ_B, marked by the thin blue line. The red line corresponds to the Lorentz-spike-like reflectivity behavior at the PDT oscillation frequency ω_0. This spike smoothens upon deviation from ω_0.

$\alpha_f \varepsilon_f^{-1}(\omega)$, results from the interplay of the positive (paralectric) and negative (ferroelectric) contributions and remains positive in the static limit in compliance with the energy conservation law. Here $\alpha_p = a_p/(a_p + a_f)$ and $\alpha_f = a_f/(a_p + a_f)$ are the relative weights of the respective layers. The adopted in-series decomposition of the total permittivity into the paraelectric and ferroelectric contributions is possible provided the thickness of the paraelectric buffer layer a_p is larger than the domain width d, so that the depolarization stray fields of the domains do not interact with the electrodes [40] (see also [41]).

The frequency dependence of $\varepsilon_{tot}(\omega)$ for the PTO/STO 30-/50-nm system is shown in Fig. 2(c). One sees (the detail of the calculations are given below) that Re $\varepsilon_{tot}(\omega)$ maintains a positive value for low frequencies and reflects the presence of the oscillatory mode at ω slightly less than ω_0. As before, the dashed line depicts the behavior of Re $\varepsilon_{tot}(\omega)$ in the absence of dissipation. We thus introduce a new metamaterial operating in the THz frequency range $\varepsilon_{tot}(\omega)$ tunable by the variation of the ratio $2a_f/2a_p$.

D. Optics

The effective permittivity of a ferroelectric/paraelectric layered system is calculated as $\varepsilon_{tot}^{-1}(\omega) = \alpha_p \varepsilon_p^{-1} + \alpha_f \varepsilon_f^{-1}(\omega)$ and can be conveniently written in a standard form:

$$\varepsilon_{tot}(\omega) = \frac{\omega_{LO}^2 - \omega^2 - i\Gamma\omega}{\omega_{TO}^2 - \omega^2 - i\Gamma\omega}\varepsilon_{tot}(\infty), \qquad (10)$$

where the characteristic frequencies ω_{LO} and ω_{TO} are the analogs of the longitudinal and traversal oscillation frequencies in the polar mode spectroscopy. The former is the DW oscillation frequency, $\omega_{LO} = \omega_0$. The latter frequency can be obtained from the relation $\omega_{TO}^2/\omega_{LO}^2 = \varepsilon_{tot}(\infty)/\varepsilon_{tot}(0)$, which is the analog of the Lyddane-Sachs-Teller relation. Here $\varepsilon_{tot}^{-1}(0) = \alpha_p \varepsilon_p^{-1} + \alpha_f \varepsilon_f^{-1}$, and $\varepsilon_{tot}^{-1}(\infty) = \alpha_p \varepsilon_p^{-1} + \alpha_f \varepsilon_\parallel^{-1}$. Equation (10) describes the dispersion curve in Fig. 2(c). It clearly shows that the obtained PDT resonance mode freezes out when the frequency exceeds ω_0 and what is left are the molecular vibrations, including the polar soft-mode oscillations.

The derived dispersion relation for the dielectric permittivity provides the foundation for the description of the THz optical properties of a ferroelectric film with PDT, in particular, for finding its complex refraction index, $n(\omega) = \sqrt{\varepsilon(\omega)}$. This enables us to devise an approach for inferring the resonance properties and negative permittivity effects from the optical measurements in the sub-THz frequency band. Importantly, in the systems that we address, the typical thicknesses of the ferroelectric layer, $2a_f \simeq 10$–40 nm, and the PDT period $2d$ are both less than the wavelength of THz radiation, $\lambda \simeq 1-0.15$ mm for 0.3–2 THz. Hence, the THz wave will interact with the system hosting the PDT like with an ultrathin dielectric film endowed with the anisotropic dielectric permittivity, the latter having in- and out-of-plane components $\varepsilon_\perp$ and $\varepsilon_f(\omega)$, respectively.

E. Reflection

We consider the situation where the incident THz beam gets reflected from the dielectric substrate, STO, with dielectric permittivity $\varepsilon_p = 300 + 10i$ in the sub-THz frequency range, passing twice through the PTO ferroelectric film with PDT. To ensure the interaction of the beam with the PDT polarization, the electric field of the light should be confined to the plane of incidence; hence, the p-wave polarization geometry should be used. The experimental setup is shown in the inset in Fig. 4(a). The calculated reflectance R of such a system is shown in

the main panel of Fig. 4(a) as a function of the angle of incidence θ by the solid blue line. The plot illustrates a typical p-wave reflectance with an amplitude that nearly vanishes in the vicinity of the Brewster angle of the substrate, $\theta_B \approx \arctan(\mathrm{Re}\,\varepsilon_p)^{1/2} \simeq 86.7^\circ$. For comparison, shown in Fig. 4(a) by the blue dashed line is also the net contribution of the substrate. Note that because of the very thin thickness of the film, it is practically indistinguishable from the reflectance of the whole system. The difference between them, $\Delta R = R_0 - R \simeq 10^{-3}$, is seen only under magnification. Thus, to ensure efficient filtering of the resonance PDT signal from the background substrate contribution, one has to focus instead on the relative variance of the signal difference, $\Delta R/R_0$, usually referred to as reflectively and used to detect the tiny molecular monolayers adsorbed on the substrate [42] (see Fig. 4).

An advantage of using the reflectivity is that the value of the substrate reflectance R_0 almost vanishes at θ_B and the use of the ratio $\Delta R/R_0$ unravels the net contribution of the ultrathin film *per se*. Shown by the solid red line, the reflectivity of our system does experience drastic variation of about unity and clearly displays the Lorentz-like spike in the vicinity of θ_B. This spike is a fingerprint of the PDT resonance and can be used for its experimental identification. The complete qualitative behavior of the resonance feature is illuminated by the three-dimensional color plot of $\Delta R/R_0$ as a function of the frequency and the angle of incidence [Fig. 4(b)]. The Lorentz spike's sharp behavior gets smoothed upon the deviation from the resonance frequency.

The reflectances R and R_0 are calculated as the square of the magnitude of the corresponding Fresnel reflection coefficients, $R = |r^p_{123}|^2$ and $R_0 = |r^p_{13}|^2$. Here index p refers to the beam polarization, and indices 1, 2, and 3 correspond to the ordering of the media: the air, the film, and the substrate, respectively.

The Fresnel reflection coefficient of the substrate-deposited film is given by the expression [42]

$$r^p_{123} = \frac{r^p_{12} + r^p_{23}e^{2i\beta}}{1 + r^p_{12}r^p_{23}e^{2i\beta}}, \tag{11}$$

where

$$r^p_{ij} = \frac{\varepsilon_j\xi_i - \varepsilon_i\xi_j}{\varepsilon_j\xi_i + \varepsilon_i\xi_j}, \qquad i, j = 1, 2, 3, \tag{12}$$

are the generalized Fresnel reflection coefficients between two adjacent media and $\beta = 2\pi(2a_f/\lambda)\xi_2$ is the phase shift of the electromagnetic wave after a single pass through the film. The generalized indices of refraction ξ_i are defined via the angle of incidence θ_1 and dielectric permittivities of the media ε_i as

$$\xi_1 = \sqrt{\varepsilon_1}\cos\theta_1, \quad \xi_2 = \left(\varepsilon_\perp - \frac{\varepsilon_\perp}{\varepsilon_2}\varepsilon_1\sin^2\theta_1\right)^{1/2}, \tag{13}$$

$$\xi_3 = (\varepsilon_3 - \varepsilon_1\sin^2\theta_1)^{1/2}. \tag{14}$$

While the refraction indices ξ_1 and ξ_3 represent the customary properties of the air, $\varepsilon_1 = 1$, and substrate, $\varepsilon_3 = \varepsilon_p$, endowed with isotropic permittivities, the targeted electrodynamic response of PDT with negative capacitance is encoded in the anisotropic refraction index ξ_2 that is deduced from [43]. The latter grasps both the transversal permittivity of the film $\varepsilon_\perp$ and the effective longitudinal permittivity of PDT, $\varepsilon_2 = \varepsilon_f(\omega)$.

The described approach identifies the PDT resonance behavior by detecting the characteristic Lorentz-like spike features in the angular and frequency dependences of the reflectance. However, the developed theory of the electromagnetic response equips us with an extraordinary more advanced technique. Namely, the resonance point ω_0 where $\varepsilon_f(\omega)$ changes sign is found, with great precision from the phase map of the Fresnel coefficient r^p_{123}. The latter (unlike the real-value reflectance $R = |r^p_{123}|^2$, where the phase information is lost) is a complex quantity which is measured, for example, by the phase-resolved ellipsometry technique [44].

To develop a feasible protocol to observe the frequency domain endowed with negative ε_f let us describe the dependence $r^p_{123}(\theta)$ near the Brewster angle in the system with the ideally transparent substrate with $\mathrm{Im}\varepsilon_p = 0$. If the film were absent, the Fresnel coefficient would have been real and would have changed sign upon passing zero at $\theta = \theta_B$. Placing the film on the substrate gives the contribution, albeit very small, that pulls r^p_{123} into a complex plane, where the trajectory $r^p_{123}(\theta)$ circumflexes the zero from the positive to negative semiaxis, acquiring the phase $\pm\pi$. Equations (11)–(14), which offer a full description of the electromagnetic response, show that the direction (clockwise vs counterclockwise) of the phase rotation is determined by the sign of ε_f. The frequency ω_0 at which ε_f changes sign corresponds therefore to a particular point in the (θ, ω) plane where the phase acquires a factor of 2π when making a close loop around it and the Fresnel coefficient r^p_{123} vanishes. These zeros of the complex function $r^p_{123}(\theta, \omega)$, where the intensity of the reflected light is zero, are often called "points of absolute darkness" [45]. They are stable with respect to small variations of parameters and hence are topologically protected, and we refer to them as topological darkness points.

Figure 5(a) displays a three-dimensional (3D) color plot of the phase and amplitude of the Fresnel reflection coefficient r^p_{123} of the PDT in the 30-nm PTO film as a function of incident angle and frequency for the case of a transparent substrate with $\varepsilon_p = 300$, derived from Eqs. (11)–(14). Two topological dark points resulting from the negative permittivity are clearly visible at the manifold depicting $r^p_{123}(\theta, \omega)$. The higher-frequency point corresponds to the above-discussed sign change of ε_f . The second, lower-frequency one appears when $\varepsilon_f \simeq -\sqrt{\varepsilon_p\varepsilon_\perp}$. This manifestly illustrates the topological protection effect: the topological darkness points are not smoothed but merely shifted by dissipation. Figure 5(b) shows the same phase plot for PTO on a real STO substrate with $\varepsilon_p = 300 + 10i$. One sees that if the dissipation is sufficiently large, the darkness points merge and cease to exist; that is, the sharp Brewster-angle singularities in the phase plot get smoothened.

The obtained results and recent measurements of the negative capacitance in PDT [15] open a new area of research in the field of THz optics in ferroelectric materials. Exciting opportunities open in the area of plasmonic epsilon-near-zero (ENZ) metamaterials with the unique property that the electromagnetic wave propagates with almost no phase advance. Although such materials have been made artificially in the microwave, visible, and far-infrared spectral ranges [46], engineered ENZ structures in the THz spectral range have not been explored so far.

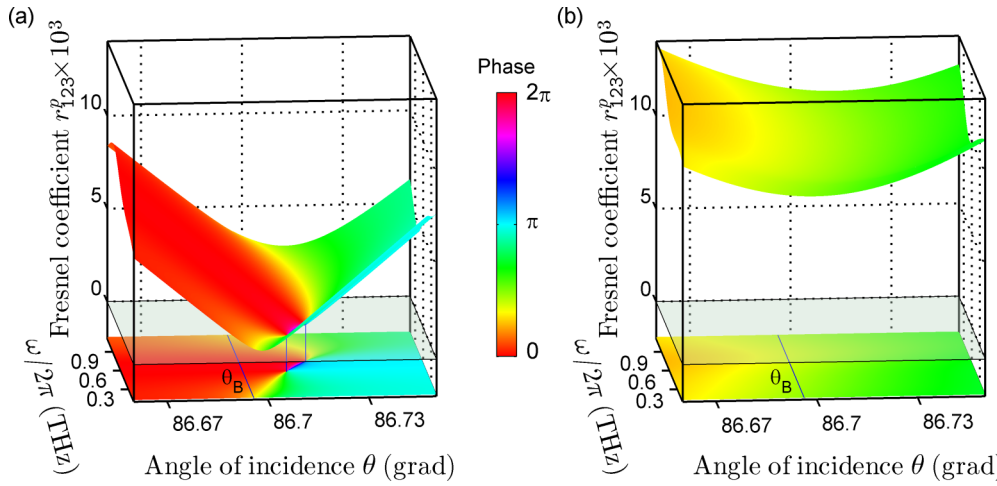

FIG. 5. The complex Fresnel reflection coefficient r^p_{123} of the PDT. (a) The 3D color plot of the phase and the amplitude of r^p_{123} as a function of the frequency ω and the angle of incidence θ for the $2a_f \simeq 30$ nm thick PTO film deposited on the transparent substrate. The substrate permittivity $\varepsilon_p = 300$ is real, with a vanishingly small imaginary part. Two topologically protected phase singularity dark points, at which $|r^p_{123}| = 0$, appear in the vicinity of the Brewster angle θ_B at frequencies where $\varepsilon_f = 0$ and where $\varepsilon_f \simeq -\sqrt{\varepsilon_p \varepsilon_\perp}$. These singular points and the inversion of the phase rotation between them that appears in blue are the fingerprint of the negative permittivity in the low-frequency region at $\omega < \omega_0$. (b) The same as (a), but for the finite-transparency STO substrate with $\varepsilon_p = 300 + 10i$. The singular phase dark points merge and annihilate. The color legend refers to both panels. The color maps of the phase distribution are shifted down from the $|r^p_{123}| = 0$ plain for convenience.

ACKNOWLEDGMENTS

This work was supported by the U.S. Department of Energy, Office of Science, Materials Sciences and Engineering Division (V.M.V.) and the European NOTEDEV-FP7-PEOPLE-ITN-2013 and ENGIMA-H2020-MSCA-RISE-2017 actions (I.L.).

APPENDIX

Calculations of the electrostatic properties of PDT in the applied field **D** generalize the zero-field Landau-Kittel calculations of PDT given in [27] with application to magnetic domains. The geometry of the system is shown in Fig. 6. The x axis is directed along the PDT texture, the y axis is parallel to the domains, and the z axis is directed across the film. Since the polarization distribution does not change along the y axis, the problem is reduced to the two-dimensional one in the xz plane. In the external field the up- and down-oriented polarization domains have different widths, d_+ and d_-, with the field-induced polarization due to DW motion being expressed via the field dependence of the asymmetry factor $\kappa = (d_+ - d_-)/2d$ as $P_{dw} = \kappa(D)P_s$, with $2d = d_+ + d_-$ being the period of the structure. Following the relation (3), we express the dielectric permittivity of the PDT as

$$\varepsilon_f = \frac{\varepsilon_\parallel}{1 - [\kappa(D)/D]P_s}. \tag{A1}$$

The linear dependence κ on D is found by minimization of the electrostatic energy of the system, considering κ as the variation parameter.

We start with the derivation of the spatial distribution of the electric fields inside the ferroelectric (f) and paraelectric (p) layers, $\mathbf{E}^{(p,f)} = (E_x^{(p,f)}, E_z^{(p,f)})$, induced by the depolarization surface charges arising at the interfaces between the f and p layers at $z = \pm a_f$. These charges, appearing due to the termination of the alternating polarization in the PDT, are conventionally presented as $\sigma_\pm(x) = \pm\vartheta(x)P_s$, where the sign-alternating function ϑ is defined as $\vartheta(x) = \pm 1$ if $x \in d_\pm$. The corresponding electrostatic potentials in the f and p layers $\nabla\varphi^{(p,f)} = -\mathbf{E}^{(p,f)}$ satisfy the Laplace equations

$$\begin{aligned} \left(\varepsilon_\parallel \partial_z^2 + \varepsilon_\perp \partial_x^2\right)\varphi^{(f)} &= 0, \\ \varepsilon_p\left(\partial_z^2 + \partial_x^2\right)\varphi^{(p)} &= 0. \end{aligned} \tag{A2}$$

The boundary conditions for the potential at the interfaces are fixed by the charges $\sigma_\pm(x)$:

$$\begin{aligned} \varepsilon_0\varepsilon_\parallel \partial_z\varphi^{(f)} - \varepsilon_0\varepsilon_p\partial_z\varphi^{(p)} &= \pm\sigma_\pm(x), \\ \varphi^{(f)} &= \varphi^{(p)}. \end{aligned} \tag{A3}$$

System (A2) with boundary conditions (A3) is solved by the Fourier-series expansion method, taking into account that

$$\sigma_\pm(x) = \pm\vartheta(x)P_s = \pm\left(\kappa + \sum_{n=1}^{\infty} p_n \cos q_n x\right)P_s, \tag{A4}$$

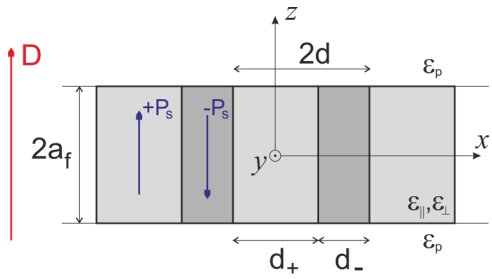

FIG. 6. The geometry of the system.

with $q_n = \pi n/d$ and

$$p_n = \frac{4}{\pi n}\sin\frac{1+\kappa}{2}\pi n. \tag{A5}$$

After straightforward calculations we obtain

$$\varphi^{(f)} = \frac{z}{a_f}\varphi_0 + P_s\sum_{n=1}^{\infty}\psi_n\frac{\sinh(\sqrt{\varepsilon_\perp/\varepsilon_\parallel}\,q_n z)}{\sinh(\sqrt{\varepsilon_\perp/\varepsilon_\parallel}\,q_n a_f)}\cos q_n x,$$

$$\varphi^{(p)} = \pm\varphi_0 - (z-a_f)\frac{D}{\varepsilon_0\varepsilon_p}$$

$$\pm P_s\sum_{n=1}^{\infty}\psi_n\exp q_n(a_f-|z|)\cos q_n x, \tag{A6}$$

where $\varphi_0 = \mp(\varepsilon_0\varepsilon_\parallel)^{-1}(D-\kappa P_s)a_f$ are the average values of the potential at the upper and lower surfaces of the ferroelectric slab and

$$\psi_n = \frac{p_n}{q_n\,\varepsilon_0\sqrt{\varepsilon_\perp\varepsilon_\parallel}\,\coth(\sqrt{\varepsilon_\perp/\varepsilon_\parallel}\,q_n a_f) + q_n\,\varepsilon_0\varepsilon_p}. \tag{A7}$$

The electrostatic energy of the system can be calculated as the integral $\sum_\pm\int dx\int[\varphi(x)]_{z=\pm a_f}d\sigma_\pm(x)$ over the surfaces of the ferroelectric layer. The integration over $\sigma_\pm$ reflects the self-consistent adiabatic charging of the surfaces, driven by the self-polarization of the system from the paraelectric state until the state with the equilibrium spontaneous polarization $\pm P_s$ is achieved inside the domains.

Taking into account the dependences given by (A6) of $\varphi(x)$ and $\sigma_\pm(x)$ on P_s, we calculate the energy per unit length of the PDT (here the factor of 2 is because of the two sides of the slab):

$$F_{el} = 2\frac{1}{2d}\int_0^{2d}dx\int_0^{P_s}[\varphi(x,P_s')]_{z=a_f}\vartheta(x)dP_s' = 2\int_0^{P_s}dP_s'\left(\varphi_0(P_s')\kappa + \frac{1}{2}P_s'\sum_{n=1}^{\infty}p_n\psi_n\right)$$

$$= \frac{2a_f}{\varepsilon_0\varepsilon_\parallel}\left(\frac{1}{2}P_s^2\kappa^2 - DP_s\kappa\right) + P_s^2\sum_{n=1}^{\infty}\frac{8d}{\pi^3n^3}\frac{\sin^2(1+\kappa)\pi n/2}{\varepsilon_0\sqrt{\varepsilon_\perp\varepsilon_\parallel}\coth(\pi n\sqrt{\varepsilon_\perp/\varepsilon_\parallel}\,a_f/d)+\varepsilon_0\varepsilon_p}. \tag{A8}$$

In the experimentally relevant limit $\sqrt{\varepsilon_\perp/\varepsilon_\parallel}\,a_f/d \gg 1$, Eq. (A8) is simplified as

$$F_{el} = \frac{2a_f}{\varepsilon_0\varepsilon_\parallel}\left(\frac{1}{2}P_s^2\kappa^2 - DP_s\kappa\right) + \frac{8}{\pi^3\varepsilon_0\varsigma\sqrt{\varepsilon_\perp\varepsilon_\parallel}}df(\kappa)P_s^2, \tag{A9}$$

where

$$f(\kappa) = \sum_{n=1}^{\infty}n^{-3}\sin^2(1+\kappa)\frac{\pi n}{2} \overset{\kappa\to0}{\simeq} \frac{7}{8}\zeta(3) - \frac{\ln 2}{4}(\pi\kappa)^2. \tag{A10}$$

Minimization of (A9) with respect to κ gives

$$\kappa = \frac{D}{P_s}\left(1 - \frac{4\ln 2}{\pi\varsigma}\left(\frac{\varepsilon_\parallel}{\varepsilon_\perp}\right)^{1/2}\frac{d}{2a_f}\right)^{-1}. \tag{A11}$$

Finally, making use of (A1), we obtain the dielectric permittivity of the PDT (4). Note that expression (4) can also be derived from the general expression for the permittivity of a paraelectric-ferroelectric system given in [47] and also from the calculations presented in [9] (see the Supplemental Material [41]).

The DW displacements in the PDT shown in Fig. 1(d) are given by $\pm x = \pm\kappa d/2$. Equating the stiffness energy of the DW displacement, $2a_f k x^2/2$, with (A9) (taken in harmonic approximation at $D=0$ and multiplying by d, i.e., using the energy for a single DW), we obtain the expression for the stiffness coefficient k, (7). The Landau-Kittel formula (5) for the domain width d is obtained by minimization of the $F_{el}+F_{dw}$ energy with respect to d at $\kappa=0$. Here $F_{dw} = (a_f/d)w_{dw}$ is the domain wall energy, calculated per unit length of the PDT, and w_{dw} is the surface energy of the DW. The spatial distribution of the electric and polarization fields in the p and f slabs is found from (A6) as $\mathbf{E}^{(p,f)} = (E_x^{(f)}, E_z^{(f)}) = -\nabla\varphi^{(p,f)}$, $\mathbf{P}^{(p)} = \varepsilon_0(\varepsilon_p-1)\mathbf{E}^{(p)}$, $\mathbf{P}^{(f)} = (P_x^{(f)}, P_z^{(f)})$, where $P_x^{(f)} = \varepsilon_0(\varepsilon_\perp-1)E_x^{(f)}$, $P_z^{(f)} = \varepsilon_0(\varepsilon_\parallel-1)E_z^{(f)} + \vartheta(x)P_s$.

[1] S. K. Streiffer, J. A. Eastman, D. D. Fong, C. Thompson, A. Munkholm, M. V. Ramana Murty, O. Auciello, G. R. Bai, and G. B. Stephenson, Phys. Rev. Lett. **89**, 067601 (2002).

[2] D. D. Fong, G. B. Stephenson, S. K. Streiffer, J. A. Eastman, O. Auciello, P. H. Fuoss, and C. Thompson, Science **304**, 1650 (2004).

[3] P. Zubko, N. Stucki, C. Lichtensteiger, and J.-M. Triscone, Phys. Rev. Lett. **104**, 187601 (2010).

[4] J. Y. Jo, P. Chen, R. J. Sichel, S. J. Callori, J. Sinsheimer, E. M. Dufresne, M. Dawber, and P. G. Evans, Phys. Rev. Lett. **107**, 055501 (2011).

[5] P. Zubko, N. Jecklin, A. Torres-Pardo, P. Aguado-Puente, A. Gloter, C. Lichtensteiger, J. Junquera, O. Stéphan, and J.-M. Triscone, Nano Lett. **12**, 2846 (2012).

[6] S. O. Hruszkewycz, M. J. Highland, M. V. Holt, D. Kim, C. M. Folkman, C. Thompson, A. Tripathi, G. M. Stephenson, S. Hong, and P. H. Fuoss, Phys. Rev. Lett. **110**, 177601 (2013).

[7] A. Yadav, C. Nelson, S. Hsu, Z. Hong, J. Clarkson, C. Schlepütz, A. Damodaran, P. Shafer, E. Arenholz, L. Dedon *et al.*, Nature (London) **530**, 198 (2016).

[8] A. M. Bratkovsky and A. P. Levanyuk, Phys. Rev. Lett. **84**, 3177 (2000).

[9] A. M. Bratkovsky and A. P. Levanyuk, Phys. Rev. B **63**, 132103 (2001).

[10] I. Kornev, H. Fu, and L. Bellaiche, Phys. Rev. Lett. **93**, 196104 (2004).

[11] V. A. Stephanovich, I. A. Luk'yanchuk, and M. G. Karkut, Phys. Rev. Lett. **94**, 047601 (2005).

[12] F. De Guerville, I. Luk'yanchuk, L. Lahoche, and M. El Marssi, Mater. Sci. Eng. B **120**, 16 (2005).

[13] P. Aguado-Puente and J. Junquera, Phys. Rev. Lett. **100**, 177601 (2008).

[14] I. A. Luk'yanchuk, L. Lahoche, and A. Sené, Phys. Rev. Lett. **102**, 147601 (2009).

[15] P. Zubko, J. C. Wojdeł, M. Hadjimichael, S. Fernandez-Pena, A. Sené, I. Luk'yanchuk, J.-M. Triscone, and J. Íñiguez, Nature (London) **534**, 524 (2016).

[16] S. Salahuddin and S. Datta, Nano Lett. **8**, 405 (2008).

[17] A. Cano and D. Jiménez, Appl. Phys. Lett. **97**, 133509 (2010).

[18] V. V. Zhirnov and R. K. Cavin, Nat. Nanotechnol. **3**, 77 (2008).

[19] D. J. Appleby, N. K. Ponon, K. S. Kwa, B. Zou, P. K. Petrov, T. Wang, N. M. Alford, and A. O'Neill, Nano Lett. **14**, 3864 (2014).

[20] A. I. Khan, K. Chatterjee, B. Wang, S. Drapcho, L. You, C. Serrao, S. R. Bakaul, R. Ramesh, and S. Salahuddin, Nat. Mater. **14**, 182 (2015).

[21] G. Catalan, D. Jiménez, and A. Gruverman, Nat. Mater. **14**, 137 (2015).

[22] T. Sluka, P. Mokry, and N. Setter, Appl. Phys. Lett. **111**, 152902 (2017).

[23] Q. Zhang, R. Herchig, and I. Ponomareva, Phys. Rev. Lett. **107**, 177601 (2011).

[24] I. Luk'yanchuk, A. Pakhomov, A. Sené, A. Sidorkin, and V. Vinokur, arXiv:1410.3124.

[25] J. Hlinka, M. Paściak, S. Körbel, and P. Marton, Phys. Rev. Lett. **119**, 057604 (2017).

[26] L. D. Landau and E. M. Lifshitz, Phys. Z. Sowjetunion **8**, 101 (1935).

[27] L. D. Landau and E. M. Lifshitz, *Electrodynamics of Continuous Media* (Elsevier, 2013), Vol. 8.

[28] C. Kittel, Phys. Rev. **70**, 965 (1946).

[29] G. Catalan, J. Seidel, R. Ramesh, and J. F. Scott, Rev. Mod. Phys. **84**, 119 (2012).

[30] B. Meyer and D. Vanderbilt, Phys. Rev. B **65**, 104111 (2002).

[31] R. T. Brierley and P. B. Littlewood, Phys. Rev. B **89**, 184104 (2014).

[32] A. S. Sidorkin, *Domain Structure in Ferroelectrics and Related Materials* (Cambridge International Science Publishing, Cambridge, 2006).

[33] G. Stephenson and K. Elder, J. Appl. Phys. **100**, 051601 (2006).

[34] E. A. Eliseev, A. N. Morozovska, S. V. Kalinin, Y. Li, J. Shen, M. D. Glinchuk, L.-Q. Chen, and V. Gopalan, J. Appl. Phys. **106**, 084102 (2009).

[35] P.-G. de Gennes and J. Prost, *The Physics of Liquid Crystals* (Oxford University Press, USA, 1995).

[36] C. Kittel, Phys. Rev. **83**, 458 (1951).

[37] N. A. Pertsev, V. G. Kukhar, H. Kohlstedt, and R. Waser, Phys. Rev. B **67**, 054107 (2003).

[38] J. Hlinka, E. Simon, C. Bogicevic, F. Karolak, and P.-E. Janolin, Phys. Rev. B **84**, 092104 (2011).

[39] E. Buixaderas, D. Nuzhnyy, P. Vaněk, I. Gregora, J. Petzelt, V. Porokhonskyy, L. Jin, and D. Damjanović, Phase Transitions **83**, 917 (2010).

[40] P. Mokrý, A. K. Tagantsev, and N. Setter, Phys. Rev. B **70**, 172107 (2004).

[41] See Supplementary Material at http://link.aps.org/supplemental/10.1103/PhysRevB.98.024107 for detailed technical derivations.

[42] V. P. Tolstoy, I. V. Chernyshova, and V. A. Skryshevsky, *Handbook of Infrared Spectroscopy of Ultrathin Films* (Wiley, Hoboken, NJ, 2003).

[43] H. Schopper, Z. Phys. **132**, 146 (1952).

[44] P. Marsik, K. Sen, J. Khmaladze, M. Yazdi-Rizi, B. P. Mallett, and C. Bernhard, Appl. Phys. Lett. **108**, 052901 (2016).

[45] V. Kravets, F. Schedin, R. Jalil, L. Britnell, R. Gorbachev, D. Ansell, B. Thackray, K. Novoselov, A. Geim, A. V. Kabashin *et al.*, Nat. Mater. **12**, 304 (2013).

[46] R. Maas, J. Parsons, N. Engheta, and A. Polman, Nat. Photonics **7**, 907 (2013).

[47] A. Kopal, P. Mokrý, J. Fousek, and T. Bahnik, Ferroelectrics **223**, 127 (1999).